Computation and Validiation of Acoustic Shielding at Realistic Aircraft Configurations

Markus Lummer* , Michael Mößner* , Jan W. Delfs†

Acoustic shielding calculations were performed for a generic test object (NACA 0012) and two realistic aircraft configurations, an Unmanned Aerial Vehicle (UAV) and a Hybrid Wing Body (HWB), and compared with experimental data, where the monopole sound source was realized using laser pulses. The agreement between calculation and experiment is good. Due to wind tunnel size limits experimental data are often restricted to the acoustic nearfield and its usability for farfield shielding predictions must be assessed numerically. In the present paper, shielding patterns were defined and its evolution with increasing distance from the geometry was studied using a simple shifting and scaling procedure. For higher frequencies, a linear scaling of the patterns with increasing distance could be established.

I. Introduction

The calculation of acoustic shielding of engine noise at realistic aircraft configurations using computational aeroacoustics (CAA) methods is a very expensive task. While it is possible to take into account arbitrary meanflow effects, the necessity to mesh the whole propagation volume of the acoustic field requires a vast amount of computational resources. Fortunately, the meanflow effects usually depend on the square of the flow Mach number and low Mach noise shielding can be calculated as scattering problem governed by the scalar wave equation. This approach is followed at DLR. This paper demonstrates exemplarily the DLR approach by presenting shielding calculations using an acoustic point source for an Unmanned Aerial Vehicle (UAV) and a Hybrid Wing Body (HWB) geometry. For validation, the calculated acoustic attenuation is compared with data from wind tunnel experiments where an acoustic point source was generated by short time laser pulses.

The research presented in this paper is part of the NATO Advanced Vehicle Technology group AVT-233 (cf. [1,2]).

The paper is structured as follows. First, to assess the influence of meanflow effects on acoustic shielding, results from 2D CAA calculations of acoustic scattering of a point source at an NACA 0012 airfoil are presented. It turns out that meanflow effects are very small for low Mach number flows and can be neglected for low to moderate frequency scattering. Then, a brief overview over the solution procedure of the acoustic wave equation is given. The convected wave equation is transformed into the classical Helmholtz equation which is subsequently solved by a Fast-Multipole Boundary Element Method (FM-BEM). Subsequently, results of shielding calculations for the UAV and HWB geometries are compared and validated with experimental data.

Due to the size of the wind tunnel models, shielding data can often be measured only in the nearfield of the scattering geometry. Therefore, the usability of these data for farfield shielding predictions must be assessed numerically, and the evolution of the shielding factor from the near- to the farfield is discussed. Shielding patterns in the observer plane are defined, whose evolution with increasing distance from the scattering geometry can be studied by a simple shifting and scaling procedure. Finally, some conclusions will be drawn.

II. Influence of Meanflow

In order to examine the influence of the meanflow field on acoustic scattering calculations for a two-dimensional NACA 0012 airfoil (chord length $c = 0.2$ m) have been performed. This section is a brief summary of section 3.2.1 from [1], where much more information can be found. Acoustic Perturbation Equations (APE) were solved with the DLR CAA-Code `PIANO` [3] based on the 4th-order finite difference DRP scheme on body fitted block structured grids and the LDDRK 4/6 scheme in time. The RANS meanflow field was calculated with the DLR CFD-Code `TAU`.

In the present computations turbulence was simulated by applying the two-equation k-omega turbulence model. The farfield conditions are: $M = 0.16$, $Re = 800,000$ (based on the chord length). The angle of attack is set to zero. The sound source is setup in a way to simulate the laser pulse used in respective experiments (see companion paper [4]). It is approximated as a point source which very locally adds heat to the acoustic computation domain. The

*Research Engineer, Department of Technical Acoustics, Institute of Aerodynamics and Flow Technology, German Aerospace Center (DLR), Lilienthalplatz 7, D-38108 Braunschweig, `markus.lummer@dlr.de`

†Head of the department of Technical Acoustics, Institute of Aerodynamics and Flow Technology, German Aerospace Center (DLR), Lilienthalplatz 7, D-38108 Braunschweig

time dependent heat flux as determined from the experiments [5] by backpropagating a time signature to an analytical point heat source is approximated with a temporal Gaussian distribution as shown in Fig. 1. The heat point source is added in such a way that it follows the meanflow as time passes by. The computation meshes shown in Fig. 2 contain

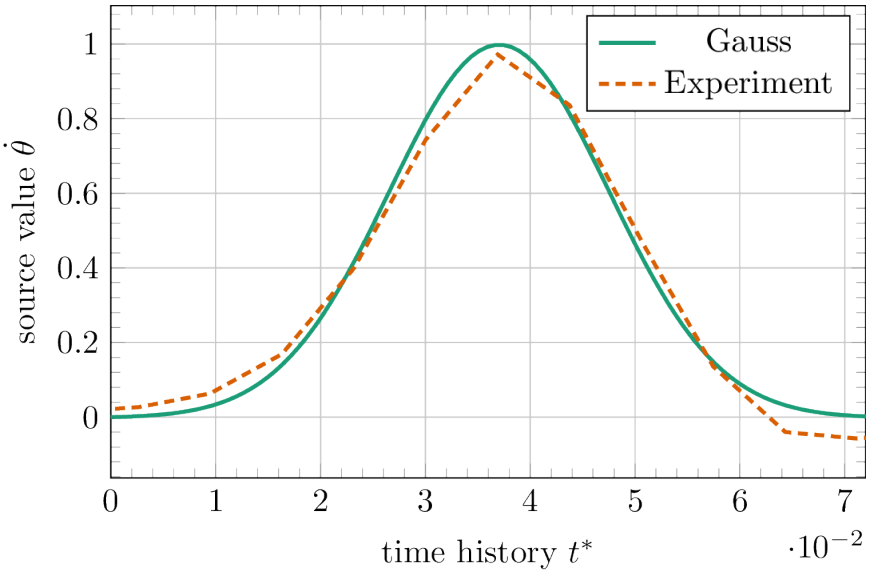

Figure 1. Heat release function as a model for the laser point source approximated by Gaussian (exp. data from [5].

about 5 Mio. grid points and are constructed such that they resolve frequencies up to 80 kHz. As an example of

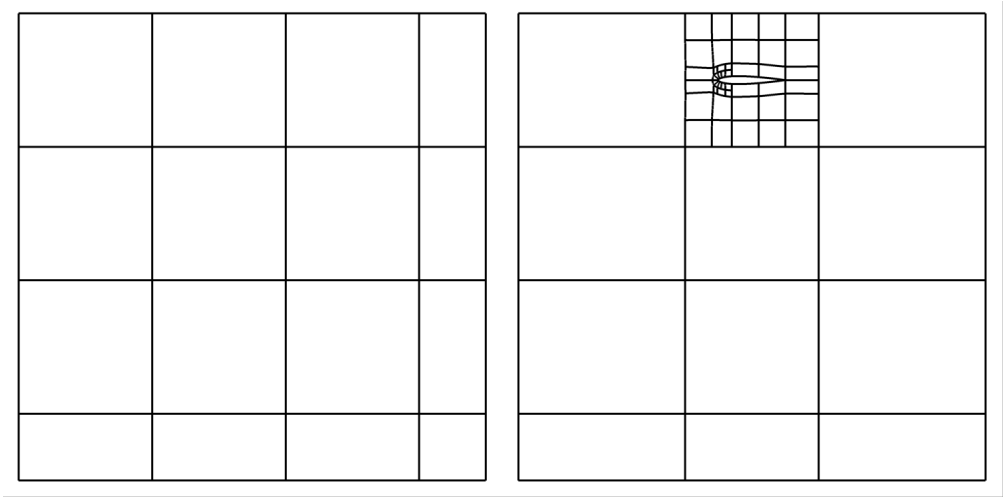

Figure 2. Block structure of CAA computation grids used for left: free field pulse simulation and right: shielded pulse simulation.

the pulse simulation Fig. 3 shows the sequence of snapshots as the pulse originating at midchord position propagates through the domain.

In a first study a setup was chosen for which significant mean flow effects could be expected, namely a case where the source is located about 10%c behind the trailing edge at a small vertical distance to the chord line, see Fig. 4. In this arrangement the sound waves hit the shear layers (particularly the airfoil upper side boundary- and then shear layer) at a very shallow angle and against the flow direction. Refraction effects are expected, which should redirect the incoming waves to the upper half. In order to study the effect of the shear three different mean flows were used:

- Viscous flow: The meanflow is computed with the RANS equations, no-slip walls and a k-ω turbulence model. This is the only case where a boundary layer develops.

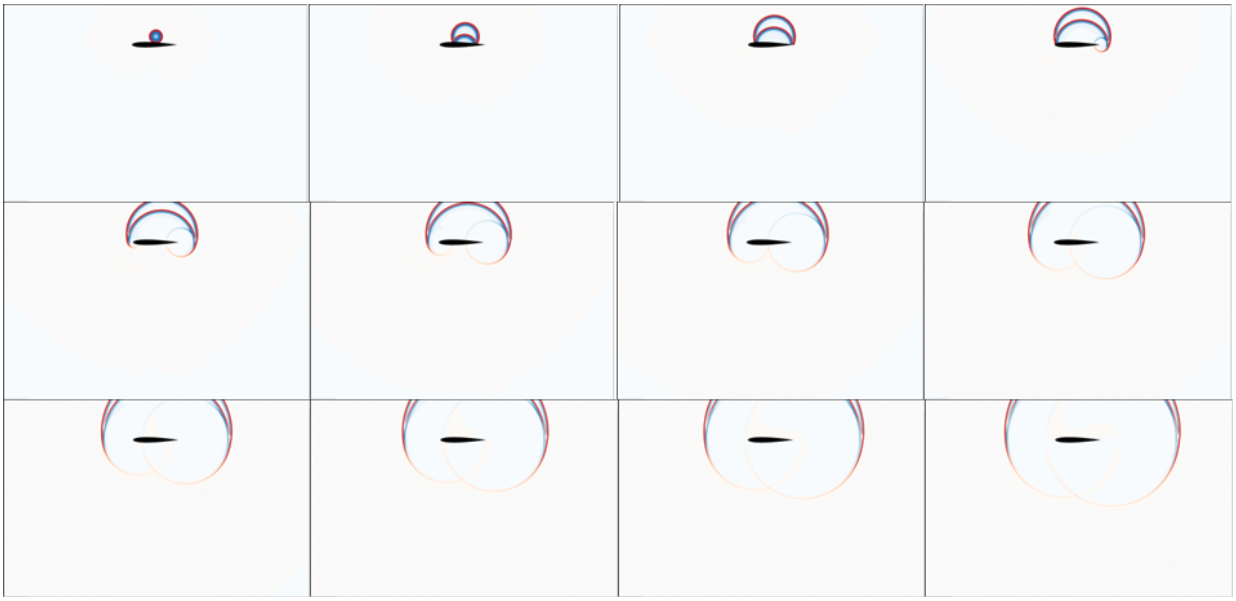

Figure 3. CAA simulation of laser induced pressure pulse in various moments.

- Slip walls: No boundary layer develops over the airfoil and hence also turbulence is ignored.
- Constant meanflow: In this case a spatially constant meanflow ($M = 0.16$) is applied.
- No mean flow: The meanflow velocity is zero everywhere.

Fig. 4 shows the directivity for three frequencies 1 kHz, 10 kHz, and 60 kHz based on the definition of the shielding level $\gamma_p = 10 \log_{10} \frac{\overline{p_s^2}}{\overline{p_i^2}}$ where p_s is the scattered pressure field and p_i the incident field (isolated point heat source). For the relatively small frequency of 1 kHz (corresponding wave length is about $\lambda/c = 1.7$) and hence a wave length longer than the airfoil the shielding is hardly influenced by the meanflow. A slight decrease of noise that can be recognized for all cases at 240° is accounted to destructive interference phenomena between the direct source and the diffraction related secondary source at the trailing edge. As the wavelength shortens to smaller values (10 kHz, $\lambda/c = 0.17$), shielding effects become visible. While they are all similar for the different meanflows, the case with viscous meanflow starts to show small differences. At 60 kHz ($\lambda/c = 0.028$) the wavelength is in the range of the boundary layer thickness. Refraction phenomena start to play a role as can be seen by the fact that the interference patterns of the viscous case differs clearly from the other cases. Even though the plot cannot provide accurate comparisons it is assured that in the directly shielded zone the viscous case shows stronger shielding levels, up to about 10 dB higher. This is credited to refraction of waves in the boundary/shear layer, which let the airfoil appear thicker than geometrically. Consequently also the reflection lobes in the upper forward direction rotate to smaller polar angles, which can only barely be seen for the 10 kHz case. In contrast, the slip wall and constant meanflow cases are very similar at all available microphone positions. The no-meanflow case is similar to the other non-viscous cases everywhere but in the direct shielding zone where it shows a different interference pattern. This accounted to the fact that the source itself is not moving in the no-meanflow case. The outcome of comparing different meanflows is that viscous meanflows will only become necessary if high frequencies are considered (wavelengths on the order of the boundary layer thickness). Otherwise using no-slip meanflows hardly provide any advantage over constant meanflows.

Another test case with more relevant shielding was studied and compared to experimental data (see also companion paper [4]), in which the source was placed right over the leading or trailing edge respectively. The shielding was investigated for zero flow and for a mean flow of Mach number $M = 0.16$ at zero angle attack of the mentioned NACA 0012 airfoil. Fig. 5 depicts the results of the shielding level as defined in Eq. (4) for the octave bands with the center frequences $f_c = 7\text{kHz}, 14\text{kHz}, 28\text{kHz}, 56\text{kHz}$ respectively. The upper row shows that at zero flow the shielding levels of the source placed above the leading edge and the trailing edge are almost equal apart from small details. It is noted that the measured and the computed shielding levels at $f_c = 56\text{kHz}$ deviate, while the correspondence is excellent at the other frequencies. This is due to a non-linear propagation effect which shows up in the considered frequency

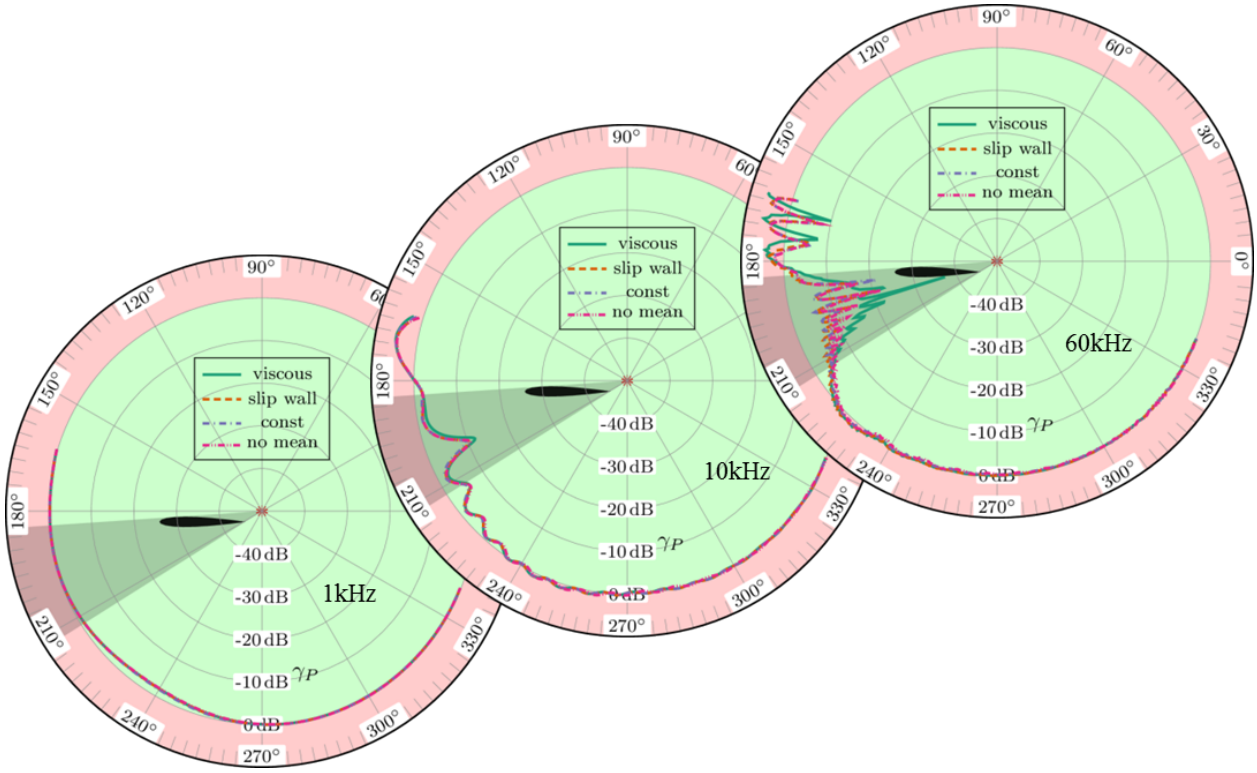

Figure 4. Frequency dependence of directivity of acoustic attenuation (shielding level) due to laser pulse initiated downstream of trailing edge for various flow field simplifications (numerical solution of APE about RANS background flow). (Fig. 3-38 from [1])

band only; the effect is discussed in detail in [5] and [4]. Under the influence of flow the picture changes. While the shielding levels remain essentially unchanged for the low frequency bands now a distinct effect occurs for the high frequency band at 56kHz seen consistently in both the experimental results as well as in the simulated results. While for the source placed over the leading edge the shielding level becomes larger in magnitude, the opposite occurs for the source placed over the trailing edge. The observed phenomenon may be explained by refraction effects. In the arrangement studied here, those sound waves which on their path to the leading or trailing edge respectively, travel at normal incidence to the streamlines/shearlayer. Thus they are hardly affected by the flow/shear. The edge-diffracted wave however, experiences very strong refraction of the lower airfoil boundary layer. Being of cardioid type pattern, the maximum amplitude of the diffracted wave will travel parallel to the lower surface and upstream (downstream) for the wave originating from the trailing (leading) edge. The diffraction wave from the trailing edge will therefore be refracted into the shadow zone (lowering the shielding effect) while the one from the leading edge will be partly captured in the boundary layer (wave guide) not being diffracted into the shadow (increasing the shielding effect). Again, as observed before, the viscous flow effect occurs for the high frequency band only, which contains frequency components with a wavelength less or equal to the boundary layer thickness. In conclusion of this section one may state that as long as the frequency considered stay in a wave length range which is larger than the boundary layer thickness at the trailing edge, the mean flow effects in the low Mach number range may be neglected and computationally much cheaper approaches are justified as will be shown in the next section.

III. Solution of the Wave Equation

For the purpose of analysing acoustic shielding effects at realistic aircraft configurations DLR's inhouse computer code FMCAS (Fast Multipole Code for Acoustic Shielding) [6, 7] is used, which implements a Fast Multipole Boundary Element Method (FM-BEM) solving the Helmholtz equation for the pressure or the acoustic velocity potential. Some brief information about the theoretical background as well as the code will be given.

In case of low Mach number mean flow fields, the shielding of engine noise can be treated as scattering problem governed by the scalar wave equation. Then, the Fourier transformed wave equation (Helmholtz equation) can efficiently be solved by boundary element methods (BEM). Low Mach number potential mean flow fields can be taken

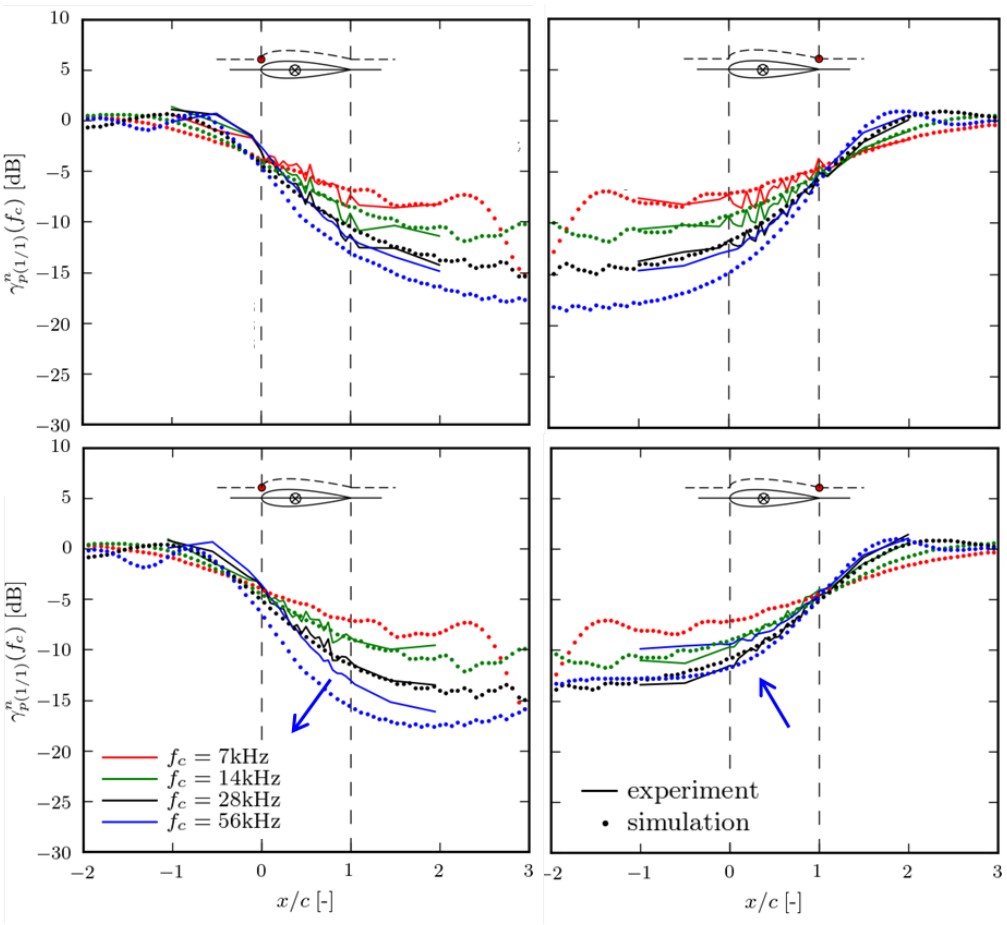

Figure 5. Effect of mean flow on shielding level for NACA 0012. Upper row: $M = 0$, lower row: $M = 0.16$. Simulation CFD: DLR TAU, CAA DLR PIANO.

into account by a so-called Taylor transformation [7, 8], where the acoustic velocity potential is multiplied by an appropriate flow dependent phase factor. The BEM is obtained by discretization of the Kirchhoff integral solution of the Helmholtz equation. The resulting system of linear equations can be solved using either direct or iterative methods. Direct methods require the storage of the full matrix while for iterative methods only the calculation of matrix-vector products must be performed. Most efficient are iterative methods where the calculation of the matrix-vector products is accelerated considerably by so-called Fast Multipole Methods (FMM) [9]. The complexity of the matrix-vector product can be reduced from $O(N^2)$ to $O(N \log N)$.

FMCAS implements a high-frequency formulation of the multi-level FMM basing on a plane wave approximation of the free-field Greens function [10]. The scattering surface is discretized using plane triangles with constant source strength. This requires a minimum resolution of 6 elements per wavelength. The meshing is performed using the open-source code `Gmsh` [11]. The iterative solvers are taken from the PETSc software library [12]. Acoustic point sources as well as source surfaces with given pressure and velocity values can be used. The code is parallelized using the OpenMP application programming interface.

IV. Experimental Approach

Shielding tests were carried out in the DLR DNW-NWB wind tunnel in Braunschweig, Germany. An acoustic point source was simulated by a laser point sound source. The scattered sound signal was splitted in its frequency components by Fourier transform and comparison of the shielded and unshielded data provided the acoustic attenuation level γ_p. The scattering of each frequency component of the laser sound source can be calculated with FM-BEM using an acoustic monopole source. The details of the experiments can be found in [1, 2] and are also published in an accompanying paper [4].

V. Sound Attenuation at Realistic Configurations

To demonstrate the achievable accuracy of the selected approach the sound attenuation in a plane 0.7 m below an UAV and a HWB configuration for a 28 kHz monopole sound source is considered. The calculated attenuation is compared with data from wind tunnel tests.

A. The DLR SACCON Geometry

The SACCON (F17E) configuration is a convex, sharped edged UAV type geometry. The wind tunnel model has the span 0.6 m and is depicted in Fig. 6. The planform of the configuration is located in the (x,y)-plane and the the origin

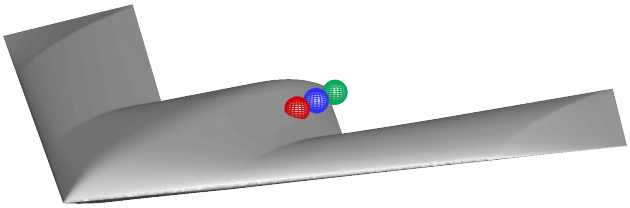

Figure 6. The SACCON F17E geometry. The colored spheres mark the source positions P1, P2, and P3.

of the computational coordinate system is very close to the nose. The position of the acoustic point source was varied along the engine jet axis located near the kink of the left trailing edge. In case of the 28 kHz monopole source the geometry was discretized with a resolution of 9 elements per wavelength resulting in about 164000 surface triangles. The iterative solver (GMRES) running on 16 cores converged in about 10 steps using about 200 seconds wall clock time. Such a fast convergence is a result of the almost convex shape of the geometry and cannot be achieved for more complex configurations.

Fig. 7 depicts the acoustic attenuation, i. e., the SPL difference between the shielded and unshielded source, for 28 kHz for four different source positions (P1-P4 marked by a small red circle). The bottom row depicts the computational results on a fine resolution grid in the observer plane $z = -0.7$ m below of the geometry. The experimental data were recorded at a much coarser grid and the top row of Fig. 7 depicts the corresponding contour plots. For direct comparison with the experimental data the pictures in the center row are generated from the computational results using the sensor locations of the experiments only. The agreement between computation and experiment is good.

B. The NASA HWB N2A Geometry

The HWB configuration is a convex-concave, sharp- and round-edged geometry which could potentially represent a large tanker or transport. The wind tunnel model has the span 1.883 m and is depicted in Fig. 8. The planform of the configuration is in the (x,y)-plane and the the origin of the computational coordinate system is very close to the nose. The position of the acoustic point source was varied along the jet axis of the left engine. In case of the 28 kHz monopole source the HWB geometry was discretized with a resolution of 6 elements per wavelength resulting in about 555000 surface triangles. The iterative solver running on 48 cores converged in about 120 steps requiring about 5200 seconds wall clock time. The SACCON and HWB calculations were executed on different machines and the performance data shall give only a quick impression of the general efficiency of the FMM code.

Fig. 9 depicts the acoustic attenuation, i. e., the SPL difference between the shielded and unshielded source, for 28 kHz for four different source positions (P1-P4 marked by a small red circle). The bottom row depicts the computational results on a fine resolution grid in the observer plane $z = -0.7$ m below of the geometry. The experimental data were recorded at a much coarser grid and the top row of Fig. 9 depicts the corresponding contour plots. For direct comparison with the experimental data the pictures in the center row are generated from the computational results using the sensor locations of the experiments only. Again, the agreement between computation and experiment is good.

For direct comparison between experiment and calculation, it is convenient to plot the shielding level below the aircraft center line in the observer plane. Fig. 10 shows the experimental and computational narrow band shielding level for 28 kHz. Although the computational curve is rather wiggly one observes a very good agreement between experiment and calculation.

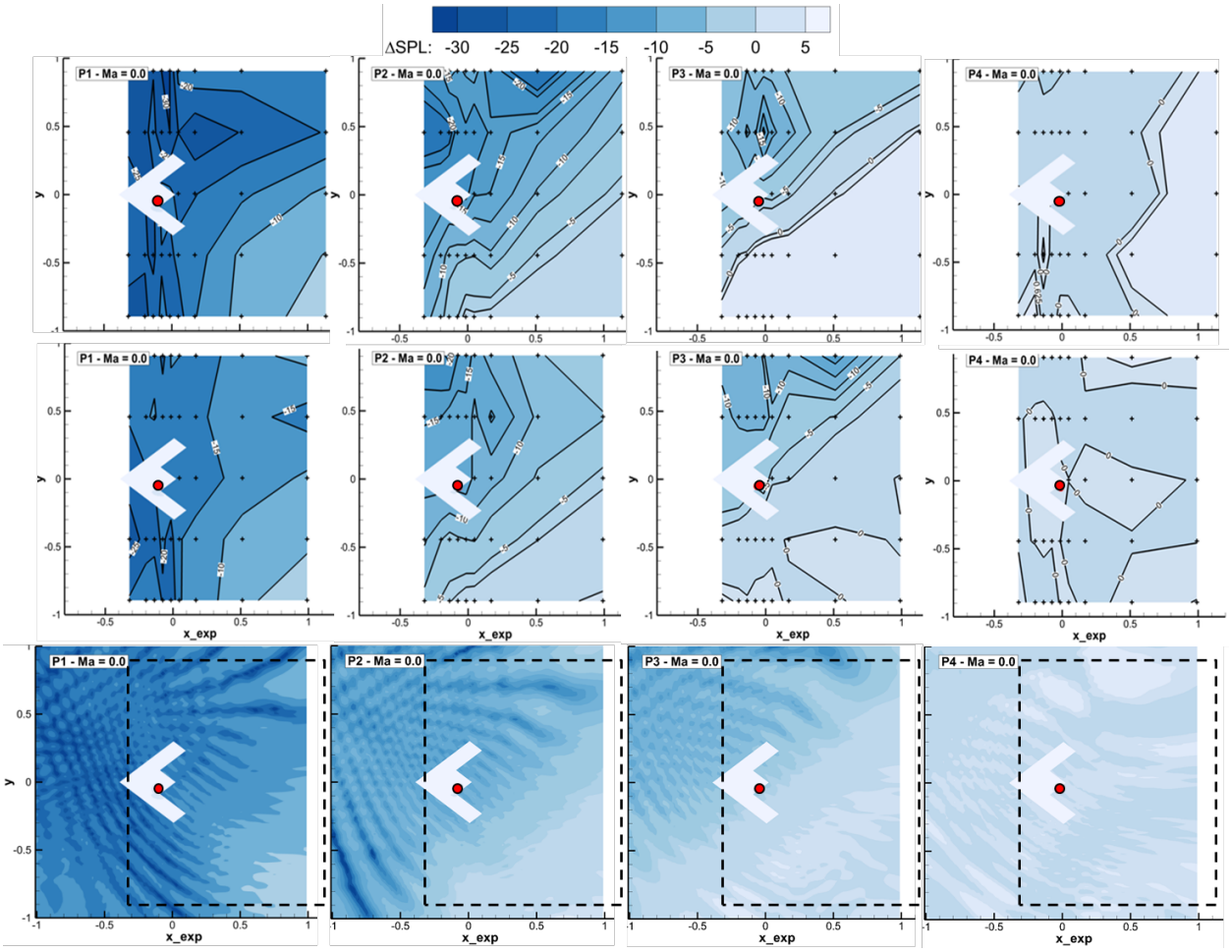

Figure 7. Comparison attenuation in plane $z = -0.7$ m below aircraft (SACCON) at 28 kHz, $M = 0$. Four source positions (P1-P4) from left to right. Top row: experiment, central row: computation at same sampling points as experiment, bottom row: densely spaced sampling points (experimental plane dashed) (Fig. 4-14 from [1]).

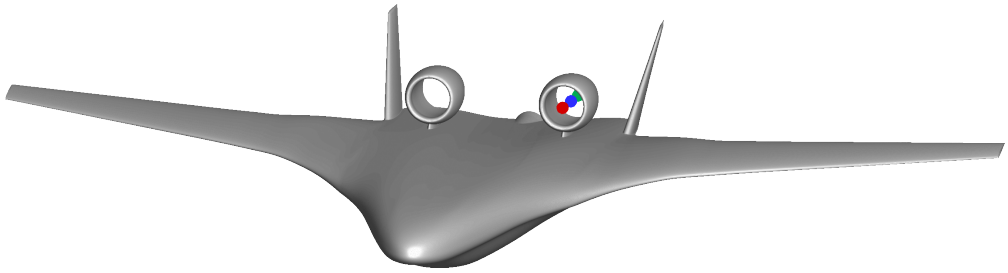

Figure 8. The NASA HWB N2A geometry. The colored spheres mark the source positions P1, P2, and P3.

VI. The Evaluation of the Shielding Factor from Near- to Farfield

Before the evaluation of the acoustic shielding from the near- to the farfield is discussed, some proposals to facilitate the interpretation of the shielding factor are made. The shielding is highly frequency dependent, but the shielding quantity should characterize the shielding properties of the object, independent on the frequency content of the (laser) source. The shielding factor $\eta(f, \boldsymbol{x})$ is defined as the ratio of the moduli of the scattered pressure $|p_s|$ and the incident

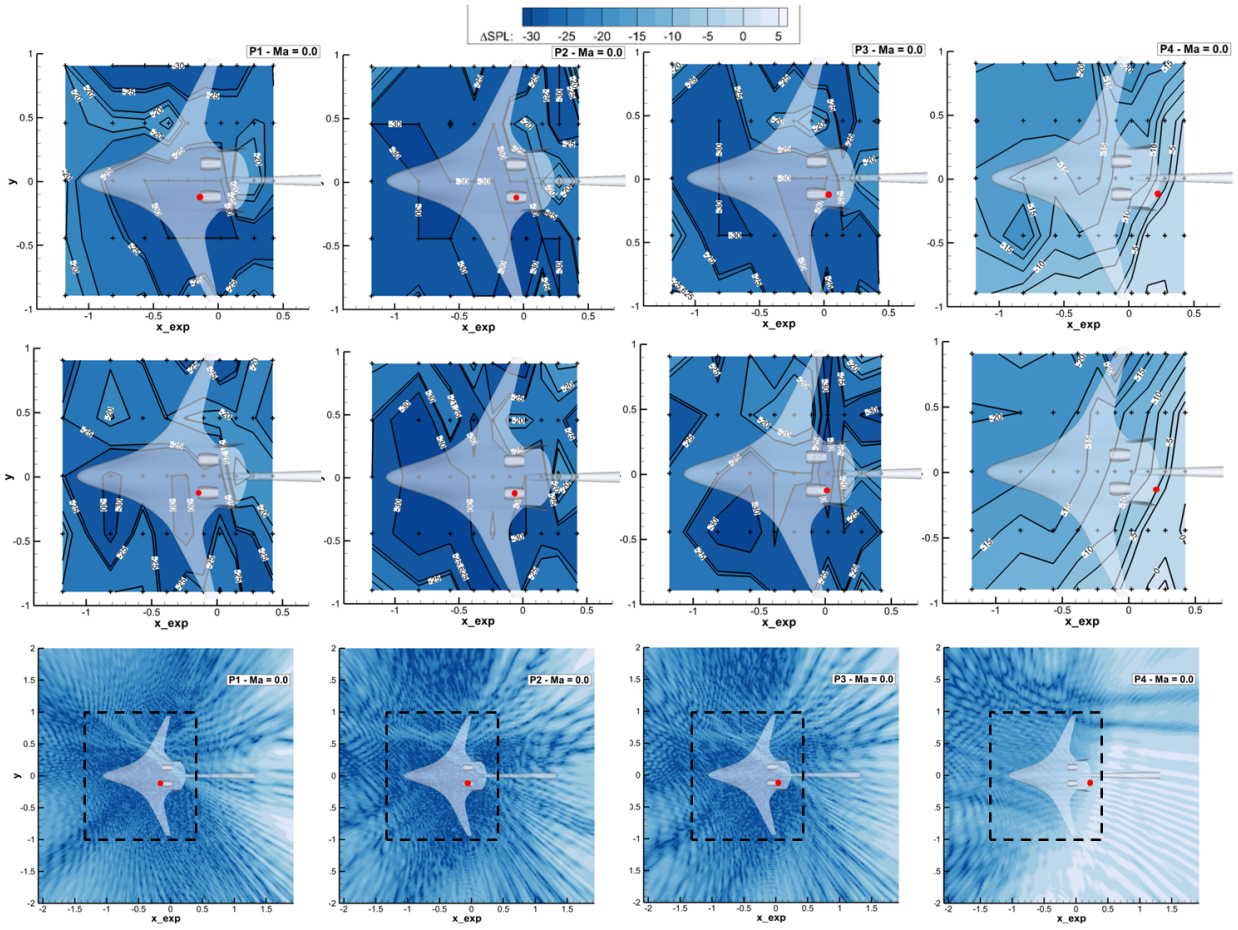

Figure 9. Comparison attenuation in plane $z = -0.7$ m below aircraft (HWB) at 28 kHz, $M = 0$. Four source positions (P1-P4) from left to right. Top row: experiment, central row: computation at same sampling points as experiment, bottom row: densely spaced sampling points (experimental plane dashed) (Fig. 4-16 from [1]).

pressure $|p_i|$

$$\eta(f, \boldsymbol{x}) \equiv \frac{|p_s|}{|p_i|}. \tag{1}$$

$\eta(f, \boldsymbol{x})$ is the so-called narrow band spectrum of the shielding factor and depends on the frequency and the spatial position. Due to the complexity of the scattering process, $\eta(f, \boldsymbol{x})$ is a highly non-smooth function of $\boldsymbol{x}$ especially at higher frequencies. In order to reduce the frequency content of the shielding factor one can define octave band averages for some frequency bands, e. g., $f_c = 7$ kHz, 14 kHz, 28 kHz, 56 kHz

$$\eta^n_{p(1/1)}(f_c) = \sqrt{\frac{\sqrt{2}}{f_c} \int_{\frac{f_c}{\sqrt{2}}}^{f_c\sqrt{2}} \eta^2(f) df}. \tag{2}$$

The chosen frequency bands between 7 kHz and 56 kHz cover well the energy content of the laser pulse source. Subsequently one can define an overall normalized shielding factor (setting $f_l = \frac{7\,\text{kHz}}{\sqrt{2}}$ and $f_u = 56\,\text{kHz}\sqrt{2}$)

$$\eta^n_{p(\infty)} = \sqrt{\frac{1}{f_u - f_l} \int_{f_l}^{f_u} \eta^2(f) df} \approx \sqrt{\frac{\sum_{\text{all } f_c} \left(\eta^n_{p(1/1)}(f_c)\right)^2 f_c}{\sum_{\text{all } f_c} f_c}}. \tag{3}$$

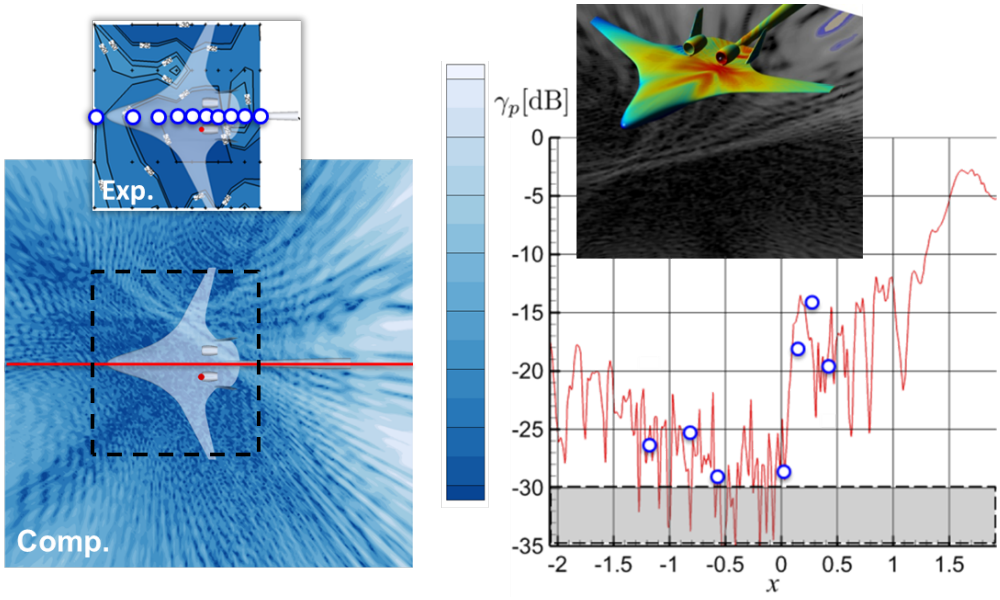

Figure 10. Shielding level γ_p below the aircraft center line in the observer plane. 28 kHz **narrow band data. Left: shielding level in the plane along with positions of sensors** 0.7 m **below the aircraft. Right: shielding level along the center line.**

In order to work with the decibel scale one can define octave band normalized shielding levels $\gamma^n_{p(1/1)}$ and an overall normalized shielding level $\gamma^n_{p(\infty)}$ according to

$$\gamma^n_{p(1/1)}(f_c) \equiv 20\log_{10}\eta^n_{p(1/1)}(f_c), \qquad \gamma^n_{p(\infty)} \equiv 20\log_{10}\eta^n_{p(\infty)}. \tag{4}$$

During experiments, usually sufficient frequency information for octave band averaging is obtained by Fourier transformation of the recorded time signals. In case of frequency domain FM-BEM calculations, however, for each octave band, several calculations must be performed at some collocation frequencies, and the integrals must be calculated by a quadrature rule. In the present case, each octave band was divided in 5 intervals and the integral in Eq. (2) was calculated using the midpoint rule. This process becomes expensive especially at higher frequencies. Moreover, the spatial smoothing effect of frequency averaging seems to be quite limited at higher frequencies, and even the band averaged data are quite wiggly. Therefore, some additional spatial smoothing can be helpful to facilitate the interpretation of the shielding data. A simple smoothing procedure for some data $f_{ij}, 0 \le i \le N_i - 1, 0 \le j \le N_j - 1$ given on a two-dimensional equidistant grid is to set

$$\bar{f}_{ij} = f_{ij} + \sigma\left(f_{i+1,j} + f_{i-1,j} + f_{i,j+1} + f_{i,j-1} - 4f_{ij}\right), \qquad 0 < i < N_i - 1, \qquad 0 < j < N_j - 1. \tag{5}$$

where σ is a small positive constant. In the calculations presented below, the smoothed quantities were the octave band normalized shielding levels $\gamma^n_{p(1/1)}$, the smoothing parameter was $\sigma = 0.2$, and the smoothing procedure Eq. (5) was applied four times.

A. Definition of Shielding Patterns

Shielding levels can form complicated patterns in the observer plane, and a procedure must be defined that allows to examine the evolution of the shielding with increasing distance of the observer plane from the geometry. It will be shown, that often characteristic patterns can be defined, whose evolution can be followed from the near- to the farfield.

One method to define such a pattern is as follows. Let the shielding levels γ be defined on an equidistant grid $\gamma_{ij}, 0 \le i \le N_i - 1, 0 \le j \le N_j - 1$. Then, define a limit value γ_B and mark all points $p_{ij} = (i, j)$ with $\gamma_{ij} < \gamma_B$. Collect points where p_{ij} and at least one of its neighbors $p_{i\pm1,j\pm1}$ are marked into a set. Usually, one finds more than one of such sets on the grid. Now, the set with the largest number of points in it is the searched shielding pattern. It has been found, that in the cases considered this procedure works very good for the highest frequency band $f_c = 28$ kHz, independent from the source position. Below, the bounding box of the shielding pattern is used to study the evolution of the shielding into the farfield. Now, some details are demonstrated for the source position P1.

B. Shielding Factor for the SACCON Geometry

Fig. 11 depicts the octave band averaged shielding levels $\gamma^n_{p(1/1)}(28\text{ kHz})$ for the SACCON configuration, the source point P1, and the observer planes $z = -0.7$ m, $z = -3.4$ m, and $z = -6.1$ m. The shielding levels were calculated on an equidistant grid with $N_i = N_j = 201$. Fig. 11a - Fig. 11c depict the raw shielding levels, Fig. 11d - Fig. 11f the smoothed ones, and Fig. 11g - Fig. 11i show the $\gamma_B = -15$ dB shielding patterns, defined in section A. It can be seen that the smoothing procedure affects the shielding level only locally and does not disturb the overall shielding pattern. It should be emphasized here that the size of the observer plane grows with increasing distance from the geometry, starting with 10×10 m^2 at $z = -0.7$ m, over 40×40 m^2 at $z = -3.4$ m to 60×60 m^2 at $z = -6.1$ m.

C. Shielding Factor for the HWB Geometry

Fig. 12 depicts the octave band averaged shielding levels $\gamma^n_{p(1/1)}(28\text{ kHz})$ for the HWB configuration, the source point P1, and the observer planes $z = -0.7$ m, $z = -3.4$ m, and $z = -6.1$ m. The shielding levels were calculated on an equidistant grid with $N_i = N_j = 201$. Fig. 12a - Fig. 12c depict the raw shielding levels, Fig. 12d - Fig. 12f the smoothed ones, and Fig. 12g - Fig. 12i show the $\gamma_B = -25$ dB shielding patterns defined in section A. Again the smoothing procedure affects the shielding level only locally, but facilitates significantly the detection of the overall shielding pattern.

D. Evolution of the Shielding Pattern

Now, the evolution of the shielding pattern with increasing distance of the observer plane from the geometry is examined. The shielding pattern can have a quite complicated structure and further simplifications are necessary. A convenient way to proceed is to refrain from details of the pattern and to look at the evolution of its bounding box in the plane. The bounding box of a pattern can be defined easily by its lower left and upper right corners $\boldsymbol{x}_0$ and $\boldsymbol{x}_1$. For the calculations it is convenient to define center and size vectors $\boldsymbol{c}_x, \boldsymbol{d}_x$ of the box and to write

$$\boldsymbol{c}_x \equiv \frac{\boldsymbol{x}_1 + \boldsymbol{x}_0}{2}, \quad \boldsymbol{d}_x \equiv \frac{\boldsymbol{x}_1 - \boldsymbol{x}_0}{2}, \quad \boldsymbol{x}_0 = \boldsymbol{c}_x - \boldsymbol{d}_x, \quad \boldsymbol{x}_1 = \boldsymbol{c}_x + \boldsymbol{d}_x. \tag{6}$$

The simplest way to describe the evolution of the box is to use a similarity transformation using a shift vector $\boldsymbol{m}(z)$ and a scaling factor $\alpha(z)$. The corner points $\tilde{\boldsymbol{x}}_i, i = 0, 1$ of the shifted and scaled bounding box read then

$$\tilde{\boldsymbol{x}}_0 = \boldsymbol{c}_x + \boldsymbol{m}(z) - \alpha(z)\boldsymbol{d}_x, \quad \tilde{\boldsymbol{x}}_1 = \boldsymbol{c}_x + \boldsymbol{m}(z) + \alpha(z)\boldsymbol{d}_x. \tag{7}$$

Now, let $\boldsymbol{x}_0$ and $\boldsymbol{x}_1$ be the corners of the pattern in the plane $z = -0.7$ and $\boldsymbol{y}_0$ and $\boldsymbol{y}_1$ the corners of the pattern box in the plane $z = -3.4$ or $z = -6.1$. Then, the shift vector $\boldsymbol{m}$ and the scaling factor α can be determined by the least squares condition

$$(\boldsymbol{y}_0 - \tilde{\boldsymbol{x}}_0)^2 + (\boldsymbol{y}_1 - \tilde{\boldsymbol{x}}_1)^2 = \min .! \tag{8}$$

The evaluation of the least squares conditions yields (details can be found in the appendix A)

$$\boldsymbol{m} = \boldsymbol{c}_y - \boldsymbol{c}_x, \quad \alpha = \frac{\boldsymbol{d}_y \cdot \boldsymbol{d}_x}{\boldsymbol{d}_x \cdot \boldsymbol{d}_x}, \quad \boldsymbol{c}_y \equiv \frac{\boldsymbol{y}_1 + \boldsymbol{y}_0}{2}, \quad \boldsymbol{d}_y \equiv \frac{\boldsymbol{y}_1 - \boldsymbol{y}_0}{2}. \tag{9}$$

Fig. 13 depicts the shifted and scaled $z = -0.7$ m bounding box for the SACCON geometry, the source position P1, and the 28 kHz band. Obviously, the transformation Eq. (7) is a good description of the evolution of the shielding pattern with z. Fig. 14 depicts the shifted and scaled $z = -0.7$ m bounding box for the HWB geometry, the source position P1, and the 28 kHz band. Again, the transformation Eq. (7) describes well the evolution of the shielding pattern with z.

One can also look at the shift $\boldsymbol{m}(z)$ and scaling $\alpha(z)$ of the patterns as functions of the distance z for different source positions. Fig. 15 depicts the scaling factor $\alpha(z)$ for the SACCON and HWB geometry. Remarkably, the scaling factor is almost a linear function of z and the same for the three source positions. The slope of $\alpha(z)$, however, is larger in case of the SACCON geometry. So far, no simple explanation have been found for this difference. Fig. 16 depicts the shift vector $\boldsymbol{m}(z)$ for the SACCON and HWB geometry. In case of the SACCON geometry, Fig. 16a, the shift vector of the shielding pattern varies strongly with the source position. Most probably, this is a consequence of the vicinity of the source positions to the surface and the relative large shift between the positions compared to the overall size of the geometry, cf. Fig. 6. In case of the HWB geometry, Fig. 16b, the shift is very small, reflecting the small distance between the source positions on the axis of the nacelle, cf. Fig. 8.

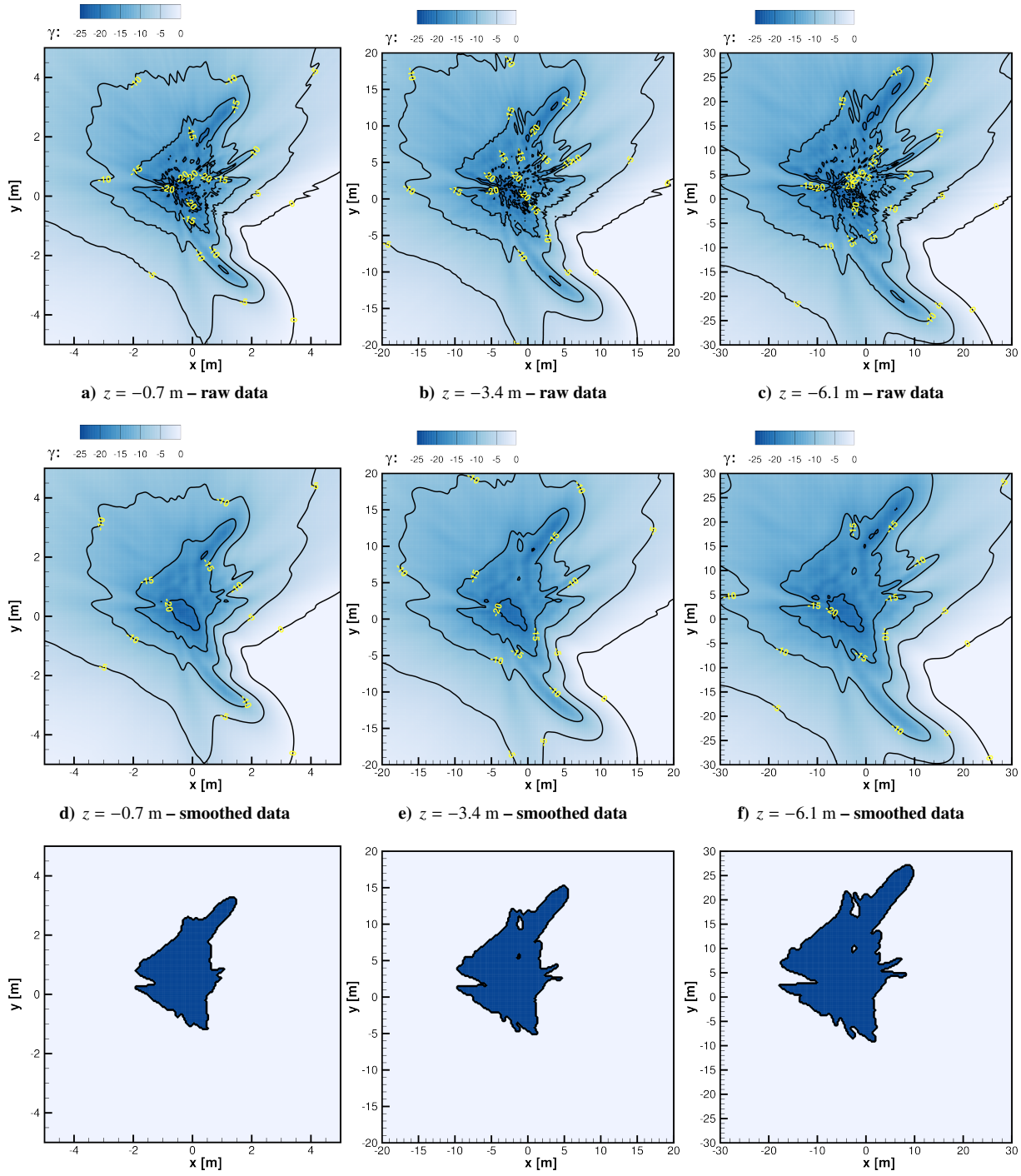

a) $z = -0.7$ m **– raw data** **b)** $z = -3.4$ m **– raw data** **c)** $z = -6.1$ m **– raw data**

d) $z = -0.7$ m **– smoothed data** **e)** $z = -3.4$ m **– smoothed data** **f)** $z = -6.1$ m **– smoothed data**

g) $z = -0.7$ m **–** $\gamma_B = -15$ dB **shielding pattern** **h)** $z = -3.4$ m **–** $\gamma_B = -15$ dB **shielding pattern** **i)** $z = -6.1$ m **–** $\gamma_B = -15$ dB **shielding pattern**

Figure 11. SACCON: octave band averaged shielding levels $\gamma^n_{p(1/1)}(28\,\text{kHz})$ for source point P1. Shielding patterns extracted from smoothed data.

VII. Conclusions

First, using 2D CAA calculations of monopole scattering at a NACA 0012 airfoil, it could be shown that viscous and mean flow effects could be neglected for small Mach number flows and small to moderate acoustic frequencies. Consequently, acoustic shielding can be calculated as scattering problem, solving the wave equation (Helmholtz equation

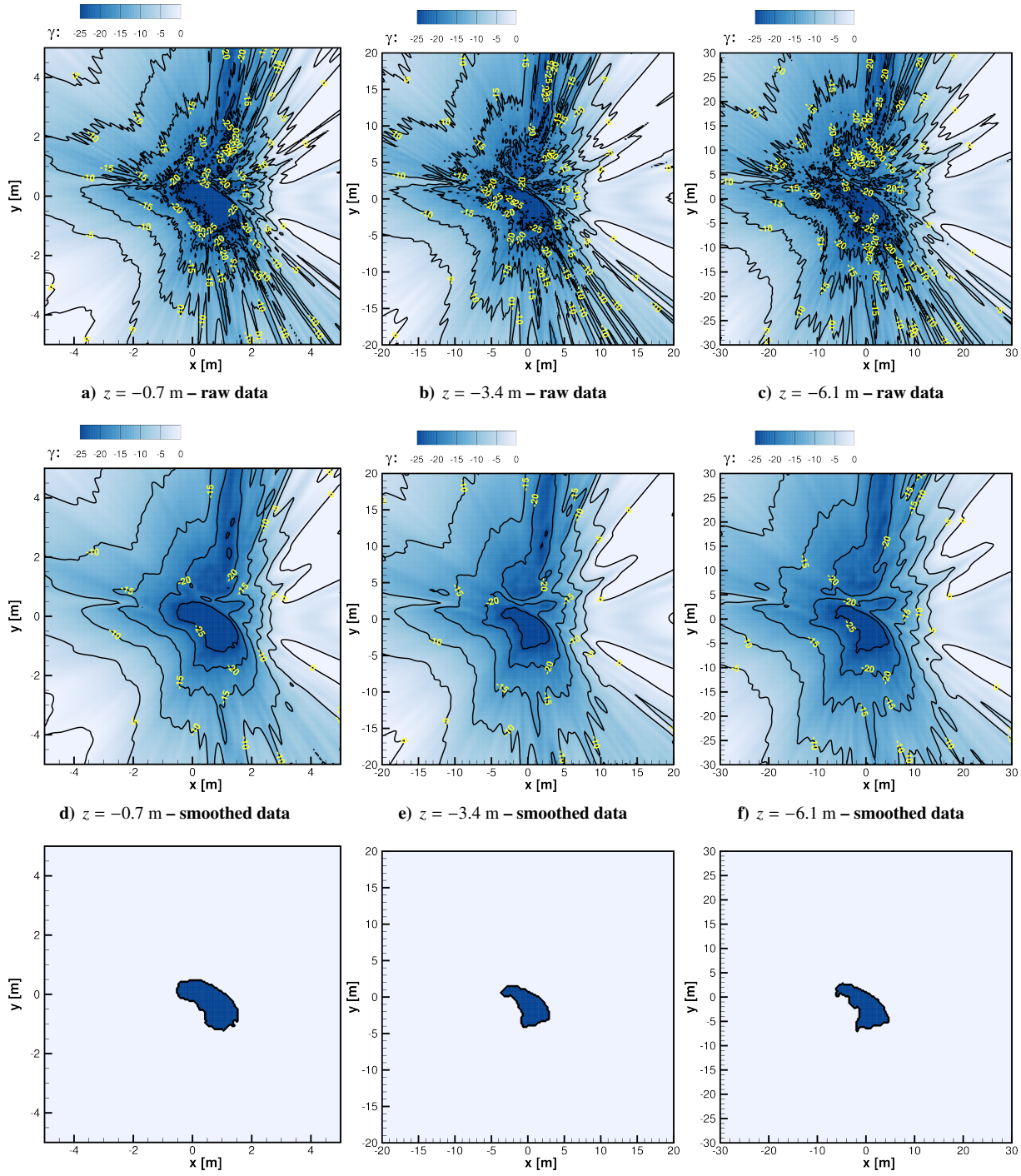

a) $z = -0.7$ m **– raw data** **b)** $z = -3.4$ m **– raw data** **c)** $z = -6.1$ m **– raw data**

d) $z = -0.7$ m **– smoothed data** **e)** $z = -3.4$ m **– smoothed data** **f)** $z = -6.1$ m **– smoothed data**

g) $z = -0.7$ m **–** $\gamma_B = -25$ dB **shielding pattern** **h)** $z = -3.4$ m **–** $\gamma_B = -25$ dB **shielding pattern** **i)** $z = -6.1$ m **–** $\gamma_B = -25$ dB **shielding pattern**

Figure 12. HWB: octave band averaged shielding levels $\gamma^n_{p(1/1)}(28\text{ kHz})$ for source point P1. Shielding patterns extracted from smoothed data.

in frequency space).

Acoustic shielding calculations were performed for two realistic aircraft configurations and compared with experimental data, where the monopole sound source was realized using laser pulses. The agreement between calculation and experiment is good. Of special interest is the evaluation of the shielding levels from the near- to the farfield. Due

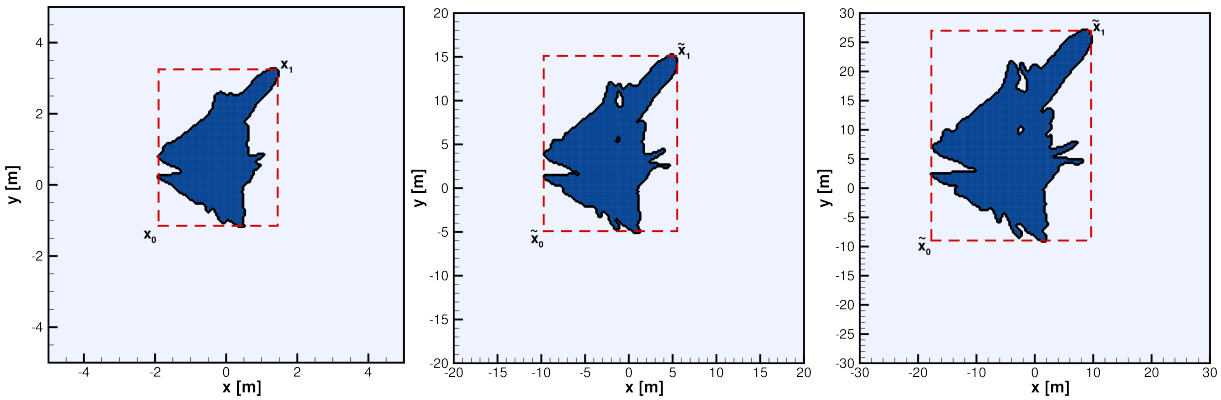

a) $z = -0.7$ m **– Original bounding box** **b)** $z = -3.4$ m **– Scaled** $z = -0.7$ m **bounding box** **c)** $z = -6.1$ m **– Scaled** $z = -0.7$ m **bounding box**

Figure 13. SACCON 28 kHz **– Scaling of bounding boxes – Source position P1**

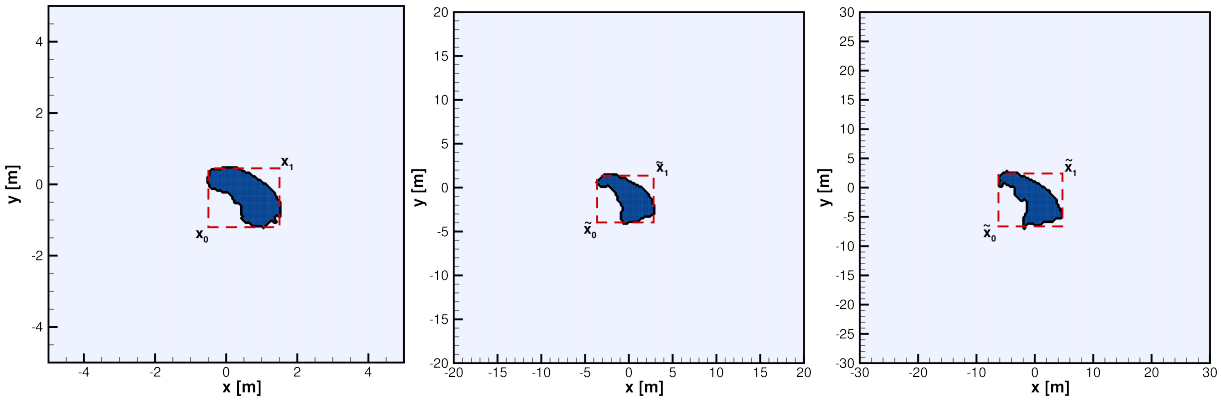

a) $z = -0.7$ m **– Original bounding box** **b)** $z = -3.4$ m **– Scaled** $z = -0.7$ m **bounding box** **c)** $z = -6.1$ m **– Scaled** $z = -0.7$ m **bounding box**

Figure 14. HWB 28 kHz **– Scaling of bounding boxes – Source position P1**

to wind tunnel size limits experimental data are often restricted to the acoustic nearfield and thus can not be used directly to assess acoustic shielding in the farfield. It is, however, possible to use shielding calculations to examine the evaluation of the shielding levels with increasing distance from the scattering geometry. First, an algorithm to define a characteristic shielding pattern has been given. Shifting and scaling of the bounding box of this pattern allowed to examine the evolution of the shielding with increasing distance of the geometry. In case of the 28 kHz octave band, the shielding pattern scales almost perfectly linear with the distance of the observer plane, independent of the source position. The slope of the scaling factor depends on the scattering geometry and no simple explanation for this can be given so far. For the 7 kHz and 14 kHz octave bands, the shielding pattern becomes more complex and automatic determination of the shielding pattern is more difficult. If, however, a pattern can be determined properly on the different planes the linear scaling with the distance also applies.

The authors acknowledge the discussions in the research group AVT-233 of NATO, within which the presented research was carried out, special thanks to NASA LARC for providing the N2A HWB geometry within AVT-233.

References

[1] Delfs, J., Thomas, R., Bahr, C., Darbyshire, O., Gély, D., Guo, Y., Hutcheson, F., Lummer, M., Mößner, M., Patience, D., and Rossignol, K.-S., "Aeroacoustics of Engine Installation on Military Air Vehicles," STO Technical Report TR-AVT-233, NATO Science and Technology Organization, 2018.

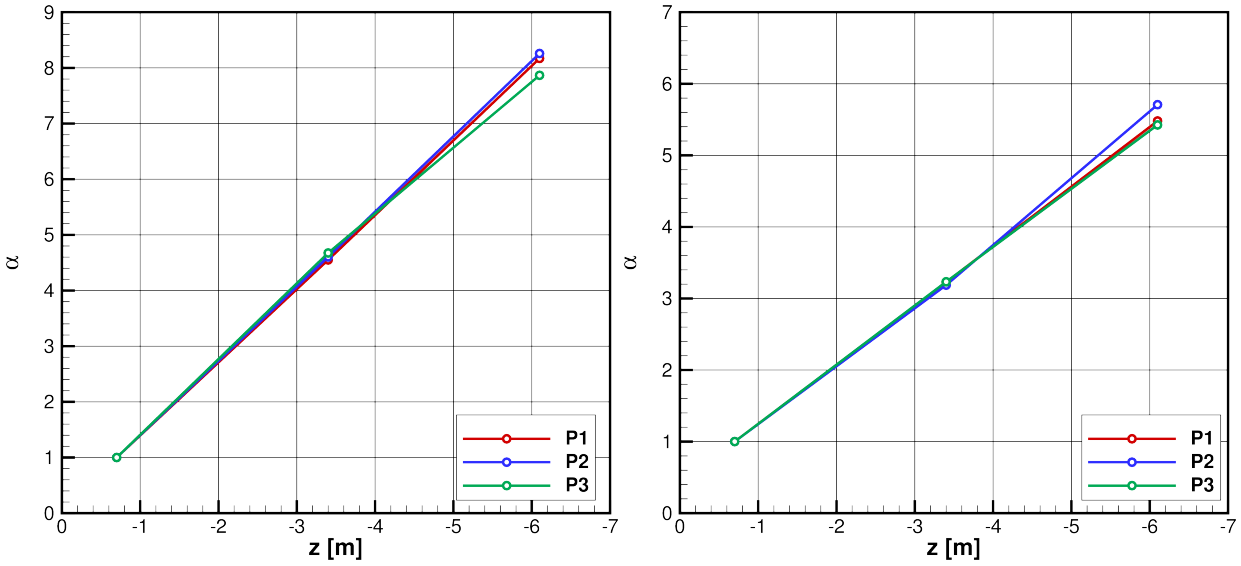

Figure 15. Bounding box scaling factor $\alpha(z)$ for the 28 kHz octave band

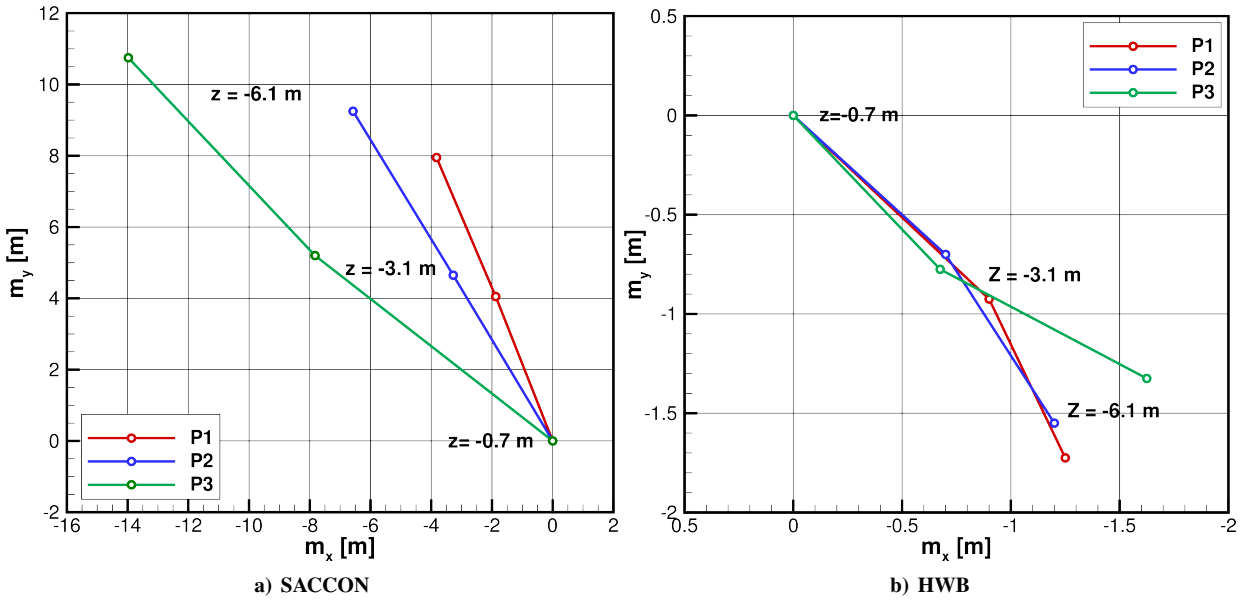

Figure 16. Bounding box shift vectors $m(z)$ for the 28 kHz octave band

[2] Rossignol, K.-S., Pott-Pollenske, M., Delfs, J., Silberman, J., and Gomez, J., "Investigating Noise Shielding by Unconventional Aircraft Configurations," *23rd AIAA/CEAS Aeroacoustics Conference, 5–9 June, 2017, Denver, Colorado, USA*, No. AIAA-2017-3195, https://doi.org/10.2514/6.2017-3195.

[3] Delfs, J. W., Bauer, M., Ewert, R., Grogger, H. A., Lummer, M., and Lauke, T. G. W., "Numerical Simulation of Aerodynamic Noise with DLRs aeroacoustic code PIANO," Tech. rep., Deutsches Zentrum für Luft-und Raumfahrt eV, Institut für Aerodynamik und Strömungstechnik, 2008, http://elib.dlr.de/118928/1/Piano_handbook_5.2_open.pdf (accessed on 14 December 2017).

[4] Rossignol, K.-S., "Experimental Investigations on Noise Shielding: Dependency on Reference Noise Source and Testing Environment," *24th AIAA/CEAS Aeroacoustics Conference, 25–29 June, 2018, Atlanta, Georgia, USA*.

[5] Rossignol, K.-S. and Delfs, J., "Analysis of the Noise Shielding Characteristics of a NACA0012 2D Wing," *22nd AIAA/CEAS Aeroacoustics Conference, 30 May – 1 June, 2016, Lyon, France*, No. AIAA-2016-2795, https://doi.org/10.2514/6.2016-2795.

[6] Lummer, M., Richter, C., Pröber, C., and Delfs, J., "Validation of a Model for Open Rotor Noise Predictions and Calculation of Shielding Effects using a Fast BEM," *19th AIAA/CEAS Aeroacoustics Conference, May 27–29, 2013, Berlin, Germany*, http://arc.aiaa.org/doi/abs/10.2514/6.2013-2096.

[7] Lummer, M., "Installation – Numerical Investigation," *Aircraft Noise Generation and Assessment*, CEAS Aeronautical Journal, submitted.

[8] Taylor, K., "A transformation of the acoustic equation with implications for wind-tunnel and low-speed flight tests," *Proceedings of the Royal Society London A*, Vol. 363, 1978, pp. 271–281.

[9] Coifman, R., Rokhlin, V., and Wandzura, S., "The Fast Multipole Method for the Wave Equation: A Pedestrian Prescription," *IEEE Antennas and Propagation Magazine*, Vol. 35, No. 3, June 1993, pp. 7–12.

[10] Rahola, J., "Diagonal Forms of the Translation Operators in the Fast Multipole Algorithm for Scattering Problems," *BIT Numerical Mathematics*, Vol. 36, No. 2, June 1996, pp. 333–358.

[11] Geuzaine, C. and Remacle, J.-F., "Gmsh: A 3-D finite element mesh generator with built-in pre- and post-processing facilities," *International Journal for Numerical Methods in Engineering*, Vol. 79, No. 11, 2009, pp. 1309–1331.

[12] Balay, S., Abhyankar, S., Adams, M. F., Brown, J., Brune, P., Buschelman, K., Dalcin, L., Eijkhout, V., Gropp, W. D., Kaushik, D., Knepley, M. G., McInnes, L. C., Rupp, K., Smith, B. F., Zampini, S., Zhang, H., and Zhang, H., "PETSc Users Manual," Tech. Rep. ANL-95/11 - Revision 3.7, Argonne National Laboratory, 2016.

A. Least Squares Fit of the Bounding Boxes

In order to examine the evolution of the size and position of a shielding pattern with increasing distance from the geometry, one can look at the evolution of its bounding box. Let the bounding box in a 1st plane be given by its corner points $\boldsymbol{x}_i, i = 0, 1$ and write

$$\boldsymbol{c}_x \equiv \frac{\boldsymbol{x}_1 + \boldsymbol{x}_0}{2}, \qquad \boldsymbol{d}_x \equiv \frac{\boldsymbol{x}_1 - \boldsymbol{x}_0}{2}, \qquad \boldsymbol{x}_0 = \boldsymbol{c}_x - \boldsymbol{d}_x, \qquad \boldsymbol{x}_1 = \boldsymbol{c}_x + \boldsymbol{d}_x. \tag{10}$$

Analogously the bounding box in the 2nd plane is defined by the corner points $\boldsymbol{y}_i, i = 0, 1$

$$\boldsymbol{c}_y \equiv \frac{\boldsymbol{y}_1 + \boldsymbol{y}_0}{2}, \qquad \boldsymbol{d}_y \equiv \frac{\boldsymbol{y}_1 - \boldsymbol{y}_0}{2}, \qquad \boldsymbol{y}_0 = \boldsymbol{c}_y - \boldsymbol{d}_y, \qquad \boldsymbol{y}_1 = \boldsymbol{c}_y + \boldsymbol{d}_y. \tag{11}$$

Now, one wishes to shift and scale the 1st box to cover the 2nd one as good as possible. In order to do so, one defines a similarity transformation by shift of the center $\boldsymbol{c}_x$ of the box by a vector $\boldsymbol{m}$ and scaling of its size by a factor α. The corners $\tilde{\boldsymbol{x}}_i, i = 0, 1$ of the transformed 1st box are then given by

$$\tilde{\boldsymbol{x}}_0 = \boldsymbol{c}_x + \boldsymbol{m} - \alpha \boldsymbol{d}_x, \qquad \tilde{\boldsymbol{x}}_1 = \boldsymbol{c}_x + \boldsymbol{m} + \alpha \boldsymbol{d}_x. \tag{12}$$

$\boldsymbol{m}$ and α can be determined from the condition that the sum of the distances of the corner points of the scaled 1st box and the 2nd box is minimum

$$(\boldsymbol{y}_0 - \tilde{\boldsymbol{x}}_0)^2 + (\boldsymbol{y}_1 - \tilde{\boldsymbol{x}}_1)^2 = \min! \tag{13}$$

The derivatives of this condition with respect to $\boldsymbol{m}$ and α are

$$(\boldsymbol{y}_0 - \tilde{\boldsymbol{x}}_0) + (\boldsymbol{y}_1 - \tilde{\boldsymbol{x}}_1) = 0, \qquad (\boldsymbol{y}_0 - \tilde{\boldsymbol{x}}_0) \cdot (-\boldsymbol{d}_x) + (\boldsymbol{y}_1 - \tilde{\boldsymbol{x}}_1) \cdot \boldsymbol{d}_x = 0. \tag{14}$$

Substitution of $\tilde{\boldsymbol{x}}_i$ and solving for $\boldsymbol{m}$ and α yields

$$\boldsymbol{m} = \boldsymbol{c}_y - \boldsymbol{c}_x, \qquad \alpha = \frac{\boldsymbol{d}_x \cdot \boldsymbol{d}_y}{\boldsymbol{d}_x \cdot \boldsymbol{d}_x}. \tag{15}$$

One sees, that the center of the scaled bounding box is the center $\boldsymbol{c}_y$ of the 2nd one, and that the scaling factor is one, if the size of both boxes is the same, i. e., $\boldsymbol{d}_y = \boldsymbol{d}_x$.